J. Fluid Mech. (1996), *vol.* 328, *pp.* 271–296

Spatio–temporal behaviour in a rotating annulus with a source–sink flow

By E. CRESPO DEL ARCO[1], P. MAUBERT[2], A. RANDRIAMAMPIANINA[2] AND P. BONTOUX[2]

[1]Departamento de Física Fundamental, UNED, Apdo. 60.141, 28080 Madrid, Spain

[2]Institut de Recherche sur les Phénoménes, Hors Equilibre, UMR 138 CNRS, and Institut de Mécanique des Fluides, 1, Rue Honnorat, 13003 Marseille, France

(Received 21 June 1994 and in revised form 3 July 1996)

The axisymmetric flows arising in a rotating annulus with a superimposed forced flow are investigated with a pseudo-spectral numerical method. The flow enters the annulus at the inner radius with a radial velocity, then develops into a geostrophic flow azimuthally directed and flanked by two Ekman (nonlinear) boundary layers, and finally exits the outer radius, with a radially directed velocity. In this study the rotation rate of the cavity is fixed and very high. When the forced flow is weak, the flow is steady. On increasing the mass flow rate, the flow evolves to a chaotic temporal behaviour through several bifurcations, which perturbs the basic spatial configuration of the flow. The first bifurcation drives the steady state into an oscillatory regime, associated with a break of symmetry with respect to the midheight of the annulus. The entry flow travels radially through the cavity as in the steady flow, but it wavers and then is alternately sucked towards each Ekman layer. The frequency of this oscillation is close to the rotation rate frequency of the cavity, which is characteristic of inertial waves in rotating flows. A second transition to a quasi-periodic regime is characterized by the appearance of a second frequency. Further increases in the flow rate lead to a period-five state, via a locking of both frequencies, and then to a chaotic motion. This second frequency is of the order of the inverse of the Ekman spin-up characteristic time, suggesting that this instability is originated by the relaxation of the perturbations in the flow field. These perturbations of the unsteady flow field are corotating vortices along the rigid boundary walls. They are excited by the entry flow and their strength diminishes with increasing radius due to the low value of the Reynolds number. The parameters characterizing the unstable flows are also consistent with this explanation. The conclusion is that in this configuration, the origin of the described dynamical behaviour is not the instability of the Ekman boundary layers, as could be expected, but the instability of the entry flow. The reason is the importance of the nonlinear inertial terms in cavities with small radius of curvature.

1. Introduction

The technological applications of source–sink flows in rotating annular cavities have motivated numerical and experimental studies on the fluid motion in these configurations. The cooling of rotating machinery may be the most obvious one. Since many physical variables depend strongly on the flow regime, it is essential to understand the different physical processes responsible for the transition of an initially laminar flow to a turbulent one.

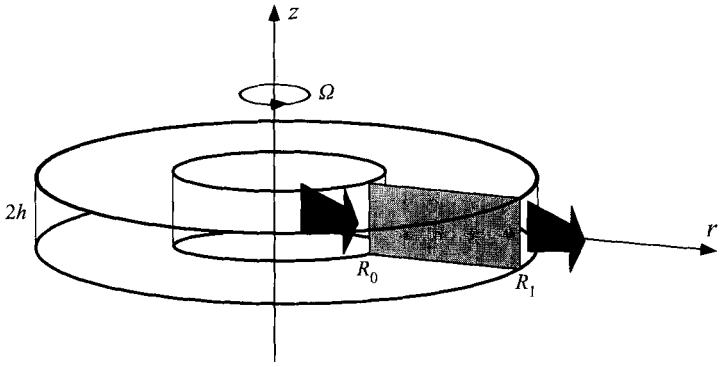

FIGURE 1. Schematic diagram of source–sink flow in the rotating cavity.

In these systems the flow is driven by the constant rotation of the walls and by a forced flow entering at the inner cylindrical wall and coming out at the outer cylinder. The laminar flow structure in this configuration can be divided into four regions: an inner source region, two separate Ekman layers, an outer sink layer, and an interior inviscid core which is bounded by the aforementioned layers. (Note that when the nonlinear inertial terms are not smaller than the Coriolis force, it is not strictly proper to retain the term 'Ekman layer' since, by definition, Ekman layers occur only when the nonlinear terms are negligible. However, the boundary layers which occur in practice are so similar to Ekman layers that, in this paper, the term 'Ekman layer' is retained even in the nonlinear case (see Bennetts & Jackson 1974; Owen, Pincombe & Rogers 1985).) By matching the solution in each region Hide (1968) found an approximate analytical solution for the basic steady flow in the cavity. This solution is axisymmetric and it is also symmetric with respect to the middle height of the cavity ($z = 0$ in figure 1). At the interior core, the flow is geostrophic and its strength is related to the mass flow rate. The Ekman layers are formed near the horizontal walls and their structure is well known (see for instance Greenspan 1969).

The experimental studies on source–sink flows in rotating annulii confirm that the basic steady flow is well approximated by the axisymmetric solution by Hide (Hide 1968; Bennetts & Jackson 1974; Owen & Pincombe 1980; Chew, Owen & Pincombe 1984; Hyun 1984). Axisymmetric and non-axisymmetric instabilities of this basic steady flow have been observed by Hide at very low mass flow and rotation rate values, in cavities with small radius: the axisymmetric instability appears as stationary concentric sheets of dye and the cause is not established, the non-axisymmetric instability shows nine short arms emerging from the source (his figure 10*e*). Bennetts & Jackson (1974) investigated the flow in the case of a rapidly rotating cavity and small radius of curvature corresponding to narrow boundary layers and strongly nonlinear regimes using a numerical method. They studied the differences between their nonlinear results and the solution of Hide and provided some experimental results to assert the computations. The experiments of Owen *et al.* (1985) were performed in a cavity with small radius of curvature for high values of the mass flow and rotation rates. Owen & Pincombe (1980) measured the velocity and compared it with theoretical predictions such as the Ekman linear solution, the length of the source and sink regions (Hide 1968) and nonlinear corrections for the geostrophic velocity (Faller 1963). Chew *et al.* (1984) obtained a numerical solution for the steady flow assuming axisymmetry and also symmetry with respect to the middle height of the cavity. Owen *et al.* (1985) compared their measurements of the velocity in the

fully turbulent flow with theoretical solutions (the model of Hide was extended, using the integral momentum techniques of von Kármán, to include laminar and turbulent flows.) The visualizations of the flow revealed that the main structures (four regions of the steady flow) are also maintained in the turbulent flow, the symmetry with respect to the midheight plane perpendicular to the axis of rotation, $z = 0$, is broken in the source region, which is the more affected in the turbulent regime. As the flow was visualized in planes (r, z), the non-axisymmetric features of the flow remain unknown.

The purpose of other experimental studies in rotating source–sink flows (see Faller 1963; Faller & Kaylor 1966; Tatro & Mollö-Christensen 1967; Caldwell & Van Atta 1970; Cerasoli 1975) was the investigation of the instabilities of the Ekman boundary layers. For this reason, the configuration is somewhat different from that used in the experiments mentioned in the previous paragraph: the flow enters the outer annulus and exits the inner annulus, and they use cavities with larger outer radius. The stability of the Ekman layer was studied by Lilly (1966) in his numerical solution of the eigenvalue problem. Theoretical investigations were carried out by Faller & Kaylor (1966). Two types of instability are associated with the Ekman boundary layer: type I, which was observed in experiments by Faller (1963), Tatro & Mollö-Christensen (1967), is a non-viscous instability with a point of inflexion in the velocity profile and the type II instability involves Coriolis and shear forces. Cerasoli (1975) has criticized Tatro & Mollö-Christensen's experiments, and his conclusion is that the wave motions interpreted as type II instability by these authors were in fact originated by probe-associated disturbances and the boundary layer waves presented by Caldwell & Van Atta (1970) were type II waves, similar to those observed by Faller & Kaylor (1966) using dye techniques.

The fact that these instabilities depend only on the local external flow field implies that they are a general feature of all rotational boundary layers and not just a singular manifestation in a particular configuration. For instance the flow patterns observed in the investigations of the von Kármán boundary layer on a disk that rotates in stationary air and on spin-up and -down experiments show the same Ekman boundary-layer instabilities (Weidman 1976). The experimental study of the flow over a disk during spin-down to rest revealed a class of circular waves in the boundary layer and, at high Reynolds numbers, the type I spiral waves are also excited with the circular waves (Savas 1987). The basic properties associated with the first Ekman-layer instability, type II, were also confirmed by Iooss, Nielsen & True (1978). A review of the results on instabilities on the boundary layers is in the paper by Faller (1991), and a shortened summary of these results is included in table 1. (A wide range of nonlinear phenomena and instabilities in rotating flows is also reported by Hopfinger & Linden 1990.)

In this paper we study the spatio–temporal behaviour of the flow upon increasing the mass flow rate. The configuration of the annulus (aspect ratio, radial outflow) that we have chosen is similar to the experiments by Owen *et al.* (1985) and models practical situations. Although the experimental results of those authors are exhaustive for the velocity profiles of the flows they do not elucidate the mechanisms of the transition to turbulence. In the present work we analyse the spatial structure of the instabilities in an attempt to identify the origin of the instabilities, whether on the Ekman layer or the entry flow, and the physical variables responsible for both mechanisms.

High spatial resolution is a requisite to describe accurately the Ekman layers and especially for a numerical study of time-dependent motions. Spectral methods have been successfully applied to compute complex time-dependent flows. The two most

Reference	Wave type	Ro	Re_c	λ^*/δ	Phase velocity V_ϕ^*/V_g^*	ε (deg.)
Measurements						
Faller (1963)	I	–	125 ± 5	10.9	–	14.5 ± 2
Tatro & Mollö-Christensen (1967)	I	$Re_c = 124.5 + 3.66\ Ro$		11.8	0.034	14.8
Tatro & Mollö-Christensen (1967)	II†	$Re_c = 56.3 + 58.4\ Ro$		27.8	0.16	0 to −8
Caldwell & Van Atta (1970)	II	–	56.7 ± 3	–	–	–
Weidman (1976)	II	–	60	20.4 ± 2.4	–	−1 to −7
Theory						
Faller & Kaylor (1966)	I	0	118	11	0.33	10 to 12
Faller & Kaylor (1966)	II	0	55	24	0.5	−15
Lilly (1966)	I	0	110	11.9	0.094	8
Lilly (1966)	II	0	55	21	0.57	−20
Iooss *et al.* (1978)	II	0	54.2	19.88	0.617	−23.3
		Ro‡	Re‡	λ^*/δ‡	V_ϕ^*/V_g^*	ε
Present results		$0.4 \geqslant Ro \geqslant 0.2$	$112 \geqslant Re \geqslant 74$	29 to 26	0.28	0

† These results have been criticized by Cerasoli (1975), who suggested that these waves were disturbances induced by the measurement probe.

‡ These parameters vary with the radial position, $-1 \leqslant r \leqslant 1$.

TABLE 1. Summary of results on Ekman layer instabilities; ϵ is the angle between the wave front and the geostrophic velocity

commonly used spectral methods are the tau and collocation versions, which differ by the test functions in the weighted residuals statement (Gottlieb & Orszag 1977; Canuto *et al.* 1987). Orszag & Kells (1980) have obtained the three-dimensional time-dependent flows in plane Poiseuille and plane Couette configurations. They solved the Navier–Stokes equations for the primitive variables (velocity–pressure) using a spectral tau-method with Fourier series in the streamwise and spanwise directions and Chebyshev polynomials in the wall-normal direction combined with a fractional time-step method. Kleiser & Schumann (1980) have proposed an influence matrix technique which has the advantage of enforcing the divergence-free velocity constraint, by solving a Poisson equation for the pressure with Dirichlet boundary conditions. Le Quéré & Pécheux (1989) have used this matrix influence technique with a spectral tau method to study the time-dependent flows in a thermally heated tall annulus. The pressure and velocity variables were expanded in truncated series of Chebyshev polynomials in both radial and axial directions. In previous works (Vanel, Peyret & Bontoux 1986; Ehrenstein & Peyret 1989; Pulicani *et al.* 1990) the flows in a two-dimensional horizontally heated cavity have been studied using spectral methods for the Navier–Stokes equations with the vorticity–streamfunction formulation, which ensured automatically the incompressibility equation. Here, we have used a spectral collocation Chebyshev method associated with an extension of the influence matrix technique used by Pulicani *et al.* (1990), to solve the Navier–Stokes equations with the vorticity–streamfunction formulation in cylindrical coordinates.

In §2 we formulate the problem and describe the numerical method. The results on the successive transitions of the observed flow are given in §3. The origin of the instabilities is discussed in §4, with particular emphasis on the structure of the flow and its time-dependent behaviour. Some calculations have also been performed without the source and sink zones by using Ekman-type solutions as boundary conditions. The results are summarized in §5.

2. Formulation of the problem

We consider the incompressible flow of a viscous fluid injected into an annular cavity of height $2h$ and depth $\Delta R = R_1 - R_0$, where R_0 and R_1 are the inner and outer radii, respectively (see figure 1). The cavity is rotating with uniform angular velocity $\boldsymbol{\Omega} = \Omega \boldsymbol{e}_z$, $\boldsymbol{e}_z$ being the unit vector in the vertical direction. We consider axisymmetric flows.

The equations governing the motion are the continuity and the Navier–Stokes equations. The scaling for the variables characterizing time, velocity and vorticity is h^2/ν, ν/h and ν/h^2. The vertical coordinate is $z = z^*/h$, $z \in [-1, 1]$ and the dimensionless radius is $\tilde{r} = r^*/h$, $\tilde{r} \in [(R_m - 1)L, (R_m + 1)L]$, where $R_m = (R_1 + R_0)/\Delta R$ is the curvature parameter and $L = \Delta R/(2h)$ the aspect ratio. (For the description of the numerical scheme we will use the cylindrical coordinates referred to the centre of the cavity: $r = 2r^*/\Delta R - R_m$, thus the integration domain $(r, z) \in [-1, 1]^2$.) The equations are solved using the vorticity and streamfunction formulation (ξ, ψ). The equations for the dimensionless variables in the rotating frame of reference are

$$\frac{\partial \xi}{\partial t} + u\frac{\partial \xi}{\partial \tilde{r}} + w\frac{\partial \xi}{\partial z} = \nabla^2 \xi + \frac{u\xi}{\tilde{r}} + \left(\frac{2v}{\tilde{r}} + \frac{2}{E}\right)\frac{\partial v}{\partial z}, \tag{2.1}$$

$$\frac{\partial v}{\partial t} + u\frac{\partial v}{\partial \tilde{r}} + w\frac{\partial v}{\partial z} = \nabla^2 v - \frac{uv}{\tilde{r}} + \frac{2u}{E}, \tag{2.2}$$

and a Poisson equation for the streamfunction ψ:

$$\nabla'^2\psi = \frac{\tilde{r}\,\xi}{L\,R_m}, \tag{2.3}$$

with

$$\nabla^2 = \frac{\partial^2}{\partial\tilde{r}^2} + \frac{1}{\tilde{r}}\frac{\partial}{\partial\tilde{r}} - \frac{1}{\tilde{r}^2} + \frac{\partial^2}{\partial z^2} \tag{2.4}$$

and

$$\nabla'^2 = \frac{\partial^2}{\partial\tilde{r}^2} - \frac{1}{\tilde{r}}\frac{\partial}{\partial\tilde{r}} + \frac{\partial^2}{\partial z^2}, \tag{2.5}$$

where (u, v, w) are the velocity components in cylindrical coordinates. The vorticity is defined by

$$\xi = \frac{\partial u}{\partial z} - \frac{\partial w}{\partial\tilde{r}} \tag{2.6}$$

and the radial and axial components of the velocity are derived from the streamfunction ψ:

$$u = \frac{L\,R_m}{\tilde{r}}\frac{\partial\psi}{\partial z}, \quad w = -\frac{L\,R_m}{\tilde{r}}\frac{\partial\psi}{\partial\tilde{r}}. \tag{2.7}$$

The Ekman number, $E = \nu/(\Omega h^2)$, is the dimensionless rotation rate of the cavity. The boundary conditions for the velocity components at the inner radius, $\tilde{r} = (R_m - 1)L$, are

$$u_0(z) = \frac{C_w}{8}\frac{R_m + 1}{R_m - 1}\cos\frac{\pi z}{2}, \quad v_0(z) = w_0(z) = 0, \tag{2.8a}$$

and at the outer radius, $\tilde{r} = (R_m + 1)L$:

$$u_1(z) = u_0(z)\frac{R_m - 1}{R_m + 1}, \quad v_1(z) = w_1(z) = 0, \tag{2.8b}$$

where $C_w = Q/(\nu\ R_1)$ is the dimensionless mass flow rate. No-slip and no-permeability conditions are imposed at the rigid walls, at $z = \pm 1$:

$$u = w = 0. \tag{2.9}$$

These walls are also subjected to uniform rotation which in our rotating system of coordinates gives the boundary condition at $z = \pm 1$:

$$v = 0. \tag{2.10}$$

2.1. *Numerical method*

The system is solved numerically using a combination of a pseudo-spectral approach in space and a second-order finite difference scheme in time (Chaouche 1990; Chaouche, Randriamampianina & Bontoux 1990). Any flow variable f and its derivative (f stands for ψ, ξ and v) are developed in truncated series of the Chebyshev polynomials at the Gauss–Lobatto points, $(r_i, z_j) \in [-1, 1]^2$:

$$r_i = \cos\frac{\pi i}{N}\ , \quad z_j = \cos\frac{\pi j}{M} \tag{2.11}$$

defined for $i = 0, ..., N$ and $j = 0, ..., M$, as follows:

$$f_{NM} = \sum_{m=0}^{M}\sum_{n=0}^{N}\tilde{f}_{n,m}\ T_n(r_i)\ T_m(z_j), \tag{2.12}$$

$$\frac{\partial^p f_{NM}}{\partial r^p} = \sum_{k=0}^{N} d_{i,k}^{(p,0)} f_{NM}(r_k, z_j, t), \tag{2.13}$$

$$\frac{\partial^q f_{NM}}{\partial z^q} = \sum_{k=0}^{M} d_{k,j}^{(0,q)} f_{NM}(r_i, z_k, t), \tag{2.14}$$

with $\tilde{f}_{n,m} = \tilde{f}_{n,m}(t)$ and $f_{NM} = f_{NM}(r_i, z_j, t)$. For the first and second derivatives, $p = 1, 2$ and $q = 1, 2$, the coefficients $d_{i,k}^{(p,0)}$ and $d_{k,j}^{(0,q)}$ are given by Ouazzani (1984) (see also Ehrenstein & Peyret 1989).

The time scheme is semi-implicit and second-order accurate. It corresponds to a combination of the second-order backward differentiation formula for the diffusive (viscous) terms and the Adams–Bashforth scheme for the nonlinear (inertial) terms (Vanel *et al.* 1986). The solution of the system at each time step reduces to the solution of a Helmholtz-type equation for the azimuthal velocity v and of a Stokes problem for the vorticity–streamfunction (ξ–ψ):

$$\nabla^2 v^{n+1} - s v^{n+1} = F_v^{n+1}(u, v, w)^{n,n-1}, \tag{2.15}$$

$$\nabla^2 \xi^{n+1} - s\xi^{n+1} = F_\xi^{n+1}(u, v, w, \xi)^{n+1,n,n-1}, \tag{2.16}$$

$$\nabla'^2 \psi^{n+1} = \left(1 + \frac{r}{R_m}\right) \xi^{n+1}, \tag{2.17}$$

where $s = 3/(2\delta t)$ and δt is the time step. F_f^{n+1} are the source terms involving the known variables computed at the time steps $(n+1)\delta t$, $n\delta t$ and $(n-1)\delta t$. The influence matrix technique derived from the one proposed by Kleiser & Schumann (1980) and extended to the vorticity and streamfunction formulation in cylindrical coordinates is used to manage the boundary conditions for the above Stokes problem.

The solver for the Poisson–Helmholtz equations is based on the partial matrix diagonalization technique developed by Haidvogel & Zang (1979). This technique has been applied in the radial direction, due to the presence of extra terms in equations (2.4), (2.5). All the eigenvalues and eigenfunctions computed were found to be real.

3. Results

Steady and time-dependent solutions have been sought in a wide range of parameters. In table 2 some details of the steady solutions are included. The number of collocation points used for computations were: $N \times M = 40 \times 40$ in (*a*), $N \times M = 64 \times 64$ in (*b*) and (*c*), and $N \times M = 100 \times 100$ in (*d*). For the case (*e*), where Ekman type boundary conditions are imposed at the entry and exit, the solution is oscillatory and two spatial resolutions, $M = 40 \times 40$ and $N \times M = 48 \times 48$ were used in order to test the accuracy of the solution. Comparison with one steady solution obtained by Bennetts & Jackson (1974) was carried out with $N \times M = 40 \times 40$ and details are reported in (*f*) and (*g*).

The time-dependent results presented in this section were obtained for $L = 3.37$, constant rotation rate, $E = 2.24 \times 10^{-3}$, and increasing mass flow rate in the range $80 < C_w < 150$ and using $N \times M = 40 \times 40$. Two values of the curvature parameter have been used: $R_m = 1.22$, thus $\tilde{r} \in [0.74, 7.48]$, and $R_m = 5$, corresponding to $\tilde{r} \in [13.48, 20.22]$. The initial condition of the numerical simulations was generally the solution obtained for a lower C_w and is given in table 3. We also performed simulations with other initial conditions (different flow regimes) in order to check that the solution is unique. The values of the time step used in the computations

	E	Ro	$\tilde{r}$	$v(\tilde{r}, z=0)$	$v_{th}(\tilde{r}, z=0)$	Radial velocity z_{max}	Radial velocity $z_{max(th)}$	Azimuthal velocity z_{max}	Azimuthal velocity $z_{max(th)}$
(*a*)	2.24×10^{-3}	0.359	4.1	−639	−569	0.959	0.963	0.876	0.889
(*b*)	1.82×10^{-3}	0.249	4.1	−914	−846	0.973	0.974	0.920	0.921
(*c*)	1.21×10^{-3}	0.201	4.1	−1106	−1051	0.980	0.979	0.933	0.936
(*d*)	9.09×10^{-4}	0.173	4.1	−1268	−1217	0.980	0.981	0.940	0.944
(*e*)	2.24×10^{-3}	0.288	16.85	−2166	−2018	0.962	0.963	0.880	0.888
(*f*)	6.4×10^{-3}	0.363	3.363	−191	−189	0.933	0.937	0.793	0.812
(*g*)	6.4×10^{-3}	0.332	3.631	−188	−175	0.933	0.937	0.793	0.812

TABLE 2. Computational details of some solutions

C_W	Initial condition	δt	Total time t_{trans}	Type of solution	Frequencies	$\Delta v/\bar{v}$ (r_2, z_2)	$\Delta v/\bar{v}$ (r_3, z_3)	$\lvert v_{max} \rvert$
100	$C_w = 85$	3.425×10^{-6}†	–	S	–	–	–	962
120	$C_w = 100$	3.425×10^{-6}‡	1.5	$P1$	80.8	0.52/781	0.015/796	1030
132	$C_w = 120$	3.425×10^{-5}	3.17 (1.4)	QP	81.3/11.9	1.09/852	0.24/873	1086
135	$C_w = 132$	3.425×10^{-5}	1.54 (0.5)	$P5$	85.2/16.7	1.10/868	0.36/892	1102
136	$C_w = 135$	3.425×10^{-5}	2.06	NP	–	–	–	–

† $\delta t = 3.425 \times 10^{-6}$ up to $t = 0.206$ and $\delta t = 3.425 \times 10^{-5}$ after this time

‡ $\delta t = 3.425 \times 10^{-6}$ up to $t = 0.617$ and $\delta t = 3.425 \times 10^{-5}$ after this time

TABLE 3. Computational details of some solutions

were $3 \times 10^{-6} < \delta t < 4 \times 10^{-5}$ and the optimal value for an oscillatory solution was $\delta t = 3.4 \times 10^{-5}$, e.g. $\delta t \sim T/360$, where $T = 1/f$ is the period (see table 3). The total time for the computation of the solution together with an estimate of the transient to stabilize oscillations (t_{trans}) are also given in table 3.

The dynamical behaviour was investigated by noting the time history of the vorticity and the streamfunction at four locations in the cavity, denoted with subindices 1, 2, 3, 4, and with coordinates $(r_1, z_1) = (0.85, 0.89)$, $(r_2, z_2) = (0, 0.89)$, $(r_3, z_3) = (0, 0)$, $(r_4, z_4) = (-0.89, 0.89)$ (these coordinates correspond to some Gauss–Lobatto Chebyshev points, and are referred to the centre of the cavity, thus $(r_i, z_i) \in [-1, 1]^2$). Points 1, 2 and 4 are near the horizontal wall (at the sink region, at the centre and at the source region respectively), and point 3 is at the centre of the cavity.

Details of the solutions are presented in table 3. As the mass flow rate is increased, the solution becomes time-dependent and the frequency of the motion is indicated. Some significant magnitudes of the variables are also given for some characteristic solutions: the time dependence of the azimuthal velocity at points 2 and 3 of the cavity is represented by its temporal amplitude, $\Delta v = v_{max} - v_{min}$, and its mean value, $\bar{v}$; the value of the maximum azimuthal velocity in the cavity is given at an arbitrary instant, $|v_{max}| = \max [v(r_i, z_j)]$, with $(r_i, z_j) \in [-1, 1]^2$.

All the time-dependent results presented here (§§3 and 4) were obtained using $N \times M = 40 \times 40$ collocation points. (With this resolution there are eight collocation points between the wall and the vertical coordinate for which the radial velocity is zero, $z^* \simeq \pi\delta$ for $E = 2.24 \times 10^{-3}$; using $N \times M = 48 \times 48$ there are ten points.) The accuracy of this spatial resolution was tested in a cavity with $R_m = 5$ and using Ekman boundary layer profiles as boundary conditions at the inlet and outlet. For $C_w = 467$ and $E = 2.24 \times 10^{-3}$ we obtained two solutions using $N \times M = 40 \times 40$ collocation points in one case and 48×48 collocation points in the other. The spectral coefficients of the streamfunction defined by equation (2.14), $\tilde{\psi}_{n,m}$, are a good measurement of the accuracy of the spatial resolution. The minimum and maximum coefficients in each expansion, $\min(\tilde{\psi}_{n',m'})/\max(\tilde{\psi}_{n,m})$ with $n, n' \in [0, N]$ and $m, m' \in [0, M]$, are $1.3124 \times 10^{-6}/305.576$ using 40×40 and $2.8505 \times 10^{-9}/305.577$ using 48×48. The frequency of the oscillatory motions obtained with these resolutions are $f = 456$ and $f = 452$ respectively, i.e. only a 1% difference.

The important time scales in the rotating flow (see for instance Greenspan 1969) are the rotation period, $t^*_\Omega = 2\pi/\Omega$ (variables with an asterisk are dimensional), the time for vorticity to diffuse viscously to the midplane, $t^*_\nu = h^2/\nu$ and the Ekman spin-up time $t^*_E = h/(\nu\Omega)^{1/2}$, which plays a crucial role. The physical meaning of these time scales and the main dynamical concepts become clear in the spin-up transition. If one takes a body of fluid between two disks and rotates them at constant angular velocity, the initial impulsive change in the angular velocity immediately produces (for $t^* \ll \Omega^{-1}$) a Rayleigh shear layer at each disk which then starts to thicken by viscous diffusion. Within a few revolutions, $t^* \simeq \Omega^{-1}$, a quasi-steady-state Ekman boundary layer develops due to the vorticity diffusion. Superimposed on these quasi-steady motions are rapid inertial oscillations that are initially of large amplitude and propagate to the interior. (The angular frequency of inertial waves in a rotating fluid is $\omega^* = 2\Omega|\cos\theta|$, where θ is the angle between the vectorial wavenumber and the angular velocity, $\boldsymbol{\Omega}$.) As time proceeds the oscillations gradually decay in amplitude. As the conditions in the interior approach the values appropriate to the final state, the Ekman layers decay and the oscillations decay in amplitude in a time $t^* \simeq t^*_E$. At very large time of order of t^*_ν, viscous diffusion has affected the entire interior and the small residual inertial oscillations are strongly damped. The three time scales,

corresponding to the development of viscous boundary layers, the spin-up time and the viscous decay of residual effects are in our case (in dimensionless units h^2/ν): $t_\Omega = 2\pi E = 0.014$, $t_E = E^{1/2} = 0.047$, $t_\nu = 1$. The maximum angular frequency for inertial waves is 2Ω, which corresponds in our dimensionless variables to a maximum frequency $f = 2/E = 141$.

3.1. *Steady flow S*

When the rotation rate is $E = 2.24 \times 10^{-3}$, the flow is steady for $C_w \leqslant 100$. At $C_w = 100$, the flow obtained with the computations, shows the four regions mentioned before and described by Hide (1968) and observed experimentally by Bennetts & Jackson (1974) and Owen *et al.* (1985) (see figure 2).

The mass transport along the radial direction takes place entirely within the boundary layers. The radial length of the source layer, or inflow region, is larger than the sink layer, by a factor of five. This feature is characteristic of the nonlinear regime when the inertial terms are important. In the core region, the flow is geostrophic: both the radial and the axial velocities are close to zero and the flow rotates inside the cavity at slower rate than the walls. The approximate asymptotic expression for the azimuthal velocity is (Hide 1968)

$$V_g^* r^* = \frac{Q\,\Omega^{1/2}}{2\pi\nu^{1/2}}\left[\exp\left(\frac{Q(R_0 - r^*)}{12\pi R_1 h\nu}\right) + \exp\left(\frac{12\pi R_0 \nu^{1/2}\Omega^{1/2}(r^* - R_1)}{Q}\right) - 1\right]$$
$$\times\left[1 - \exp\left(\frac{z^* - h}{\delta}\right)\cos\left(\frac{h - z^*}{\delta}\right) - \exp\left(\frac{-(h + z^*)}{\delta}\right)\cos\left(\frac{z^* + h}{\delta}\right)\right]. \quad (3.1)$$

The ratio of inertial to Coriolis forces is known as the Rossby number, $Ro = V_g^*/(\Omega r^*)$, where V_g^* is the local geostrophic velocity, $\delta = (\nu/\Omega)^{1/2}$ the thickness of the boundary layer, and r^* the dimensional radial position. Hereafter we will give the Rossby number, Ro, obtained with the computed values of the azimuthal velocity at the centre of the cavity. For $C_w = 100$, the computed value at the centre, $\tilde{r} = 4.1$ and $z = 0$ is $v = -639$ and it corresponds to a strongly nonlinear flow, $Ro = 0.359$. This solution is (*a*) in table 2. We will use this solution and increase the mass flow rates in the next subsections.

We have obtained other stationary solutions for increasing rotation rates and also in a different geometry. In figure 3 the numerical results for $C_w = 75.8$ (then the resulting value of the Rossby number at the centre of the cavity, $\tilde{r} = 3.363$ is $Ro = 0.363$) are shown together with the numerical and experimental results obtained by Bennetts & Jackson (1974), for $Ro = 0.363$; the other parametric values are the same: $E = 6.4 \times 10^{-3}$, $L = 1.34$. Even though the boundary conditions at the entry and the exit are not the same, their numerical solution is reproduced almost exactly. (For the radial velocity at the entry and the exit, $u(\tilde{r} = 2.023)$, and $u(\tilde{r} = 4.703)$ they use an almost constant profile, smooth near the corners at $z = \pm 1$, while we use a cosine profile (2.8*a*).)

The characteristics of the nonlinear solution are well explained by these authors. However we include some results concerning the differences between the analytical expression for the asymptotic solution obtained by Hide (1968) and the numerical solution. The depth of the boundary layer and the Ekman solution remain good approximations as is seen in table 2 for very different parameters. However in figure 4 and in table 2 it is seen that for higher values of the Rossby number, the depth is slightly larger. The cases (*f*) and (*g*) show the same numerical solution at different $\tilde{r}$: (*f*) at the centre, and (*g*) at a slightly different radial position. The values of

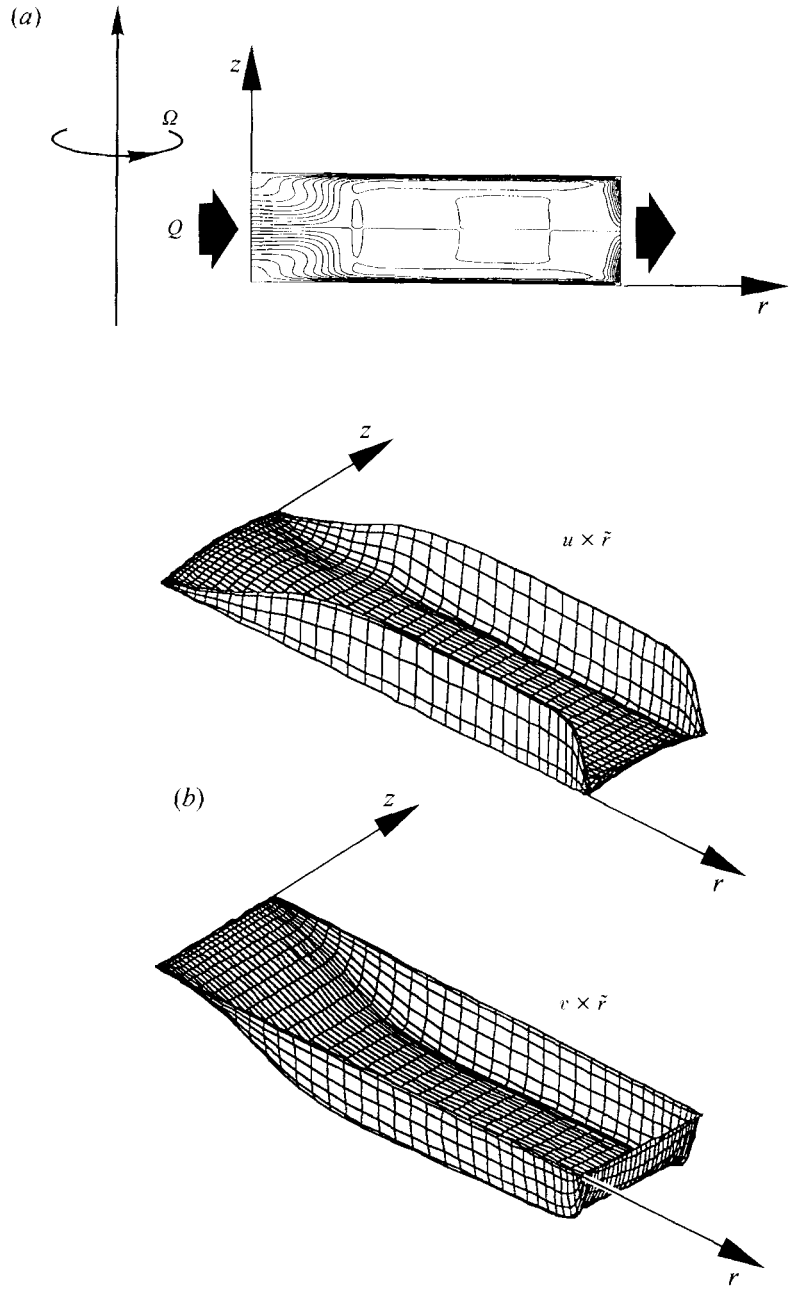

FIGURE 2. (*a*) Streamlines of the steady flow for $C_w = 100$, $E = 2.24 \times 10^{-3}$, $L = 3.37$ and $R_m = 1.22$. (*b*) Two-dimensional azimuthal and radial velocity plots: $v \times \tilde{r}$ and $u \times \tilde{r}$. Boundary conditions from equation (2.8 *a,b*) at $\tilde{r} = 0.74$ and $\tilde{r} = 7.48$ ($r = \pm 1$). $Ro = 0.359$

the Rossby numbers are obtained with the value of the velocity v at the position $\tilde{r}$ and $z = 0$. The v_{th} is the value from (3.1) predicted from the asymptotic solution of Hide (1968) at the same location. The z_{max} are the positions of the maxima of the radial and azimuthal velocity components (numerical solution) and $z_{max(th)}$ are the theoretical positions of the maximum azimuthal velocity, i.e. $z = E^{1/2}\, 3\pi/4$ and radial velocity, $z = E^{1/2}\, \pi/4$. The numerical radial velocity at the core was found

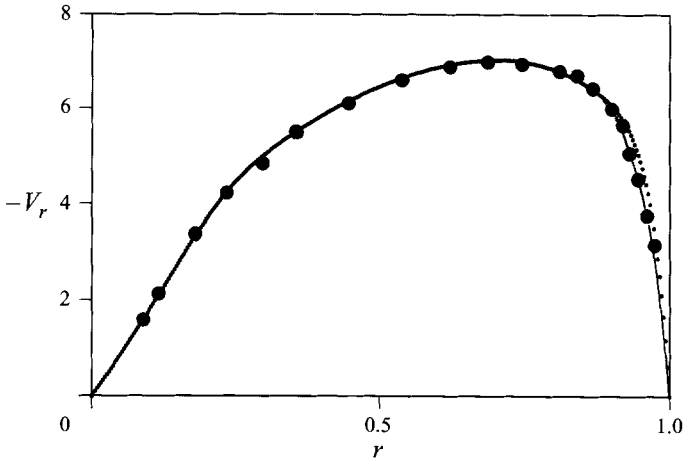

FIGURE 3. Comparison of the numerical results (···) for $C_w = 75.8$, with numerical (—) and experimental (•) results obtained by Bennetts & Jackson (1974) for $Ro = 0.363$, $E = 6.4 \times 10^{-3}$, $L = 1.34$.

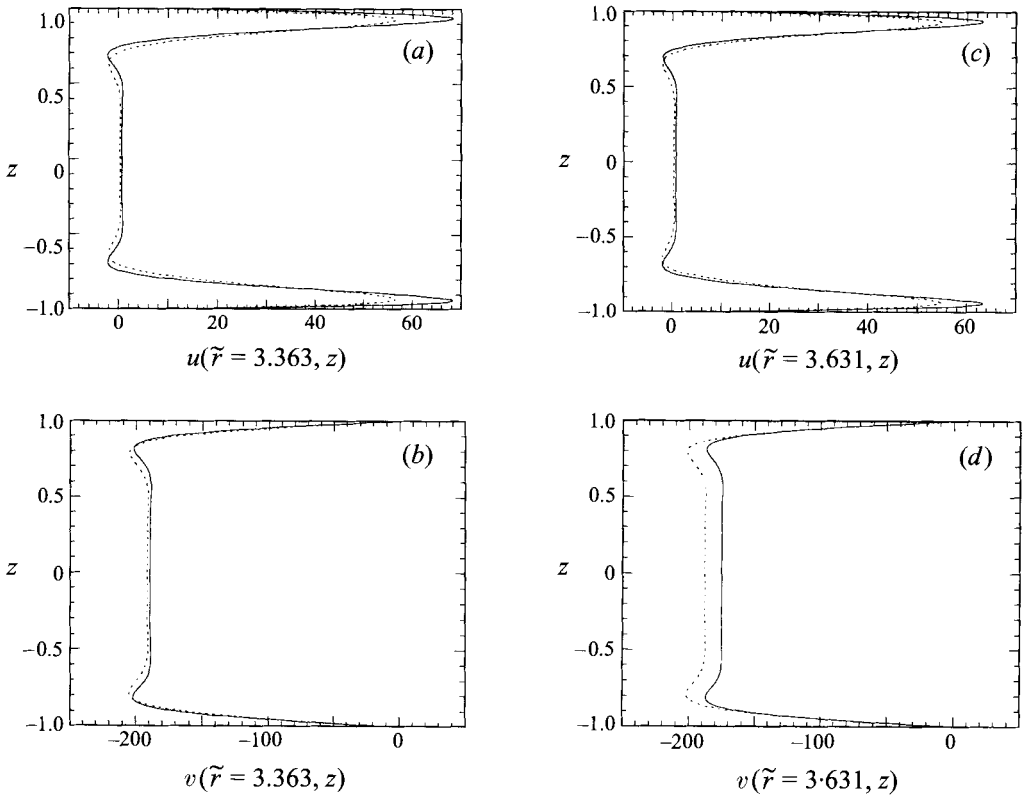

FIGURE 4. Comparison of the numerical solution (···) with the asymptotic solution (3.1) (—) obtained by Hide (1968) for the same parameters as in figure 3, at different positions: (*a*) $u(\tilde{r} = 3.363, z)$; (*b*) $v(\tilde{r} = 3.363, z)$; (*c*) $u(\tilde{r} = 3.631, z)$; (*d*) $v(\tilde{r} = 3.631, z)$.

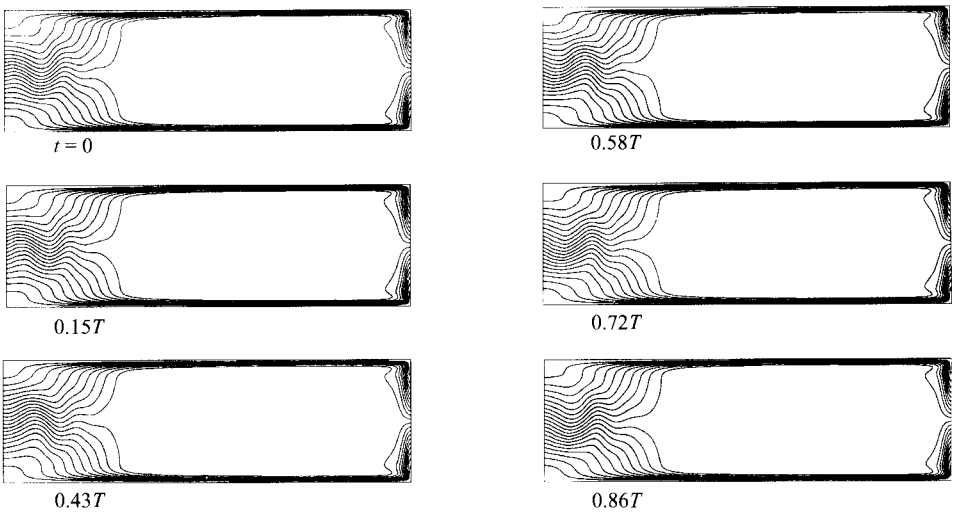

FIGURE 5. Instantaneous plots of the iso-streamfunction lines of the oscillatory flow at different time steps. $C_w = 120$, $E = 2.24 \times 10^{-3}$, $L = 3.37$ and $R_m = 1.22$. The period is $T = 0.0124$ and at the centre of the cavity $Ro = 0.433$. Boundary conditions from (2.8*a*,*b*) at $\tilde{r} = 0.74$ and $\tilde{r} = 7.48$ ($r = \pm 1$).

to be zero. Also, the radial velocity in the boundary layers is weaker than in the theory due to inertial terms as shown in figure 4. Associated with this fact, it is noted that the velocity at the core is underestimated by the analytical solution (3.1). The difference between these values increases at higher Rossby number and in that case results from nonlinear effects.

3.2. *Transition* $S \rightarrow P1$

Using the solution of figure 2 as initial condition, the mass flow rate was increased and the same values of all the other parameters were kept. At $C_w = 120$ the motion is oscillatory with a frequency $f = 80.8$. The corresponding period, $T = 1/f = 0.0124$ is close to the rotation period $t_\Omega = 0.014$. A long transient time is needed to reach the stabilized time-dependent solution, i.e. $t_{trans} = 1.5$, larger than the viscous time, $t_\nu = 1$.

The transition to periodic flow is associated with a break in the symmetry of the flow pattern with respect to the midheight of the cavity, as can be observed comparing the plots of the streamfunction in figures 2 and 5. In order to display the oscillatory behaviour the iso-ψ plots are represented in figure 5 at different time steps during a period. At the source region the entry flow wavers near the horizontal middle plane, $z = 0$, and its wavelength is about the size of the source region, $\lambda^* \sim \Delta R/7.5$. During one period the wavy motion flows alternately towards the top and the bottom Ekman layers. The Ekman boundary layers do not seem to be disturbed by the instability (see figure 5). The velocity at the centre of the cavity is $v = -796$ ($Ro = 0.433$).

The flow is oscillatory, $P1$, when C_w is increased to 125 and 130, and the corresponding frequencies are $f = 80.3$ and 80.9. These frequencies are about the same as the frequency obtained at $C_w = 120$. During the transient to the oscillatory solution at $C_w = 130$, we have observed a modulation (about $f/6$) on the signals of the variables at the Ekman layers, $\psi(t; r_i, z_i)$, with $i = 1, 4$. The amplitude of the modulation decreases with time and the final solution is oscillatory. This modulation was not observed at other locations, or for $C_w = 120$ and 125.

3.3. *Transition* $P1 \rightarrow QP$

On increasing the mass flow rate C_w up to 132, the power spectra reveal a quasi-periodic dynamic behaviour, denoted QP, with two incommensurate frequencies, f and f', 81.3 and 11.9, respectively ($T = 0.0123$ and $T' = 0.084$).

The instantaneous iso-ψ plots in figure 6 do not reveal substantial differences with respect to the flow in the periodic regime, $P1$. However, the wavy flow observed at the entry has a larger amplitude and a slightly shorter wavelength than the periodic instability at $C_w = 120$. Analysis of the power spectra from the streamfunction at different locations in the cavity in figure 7, shows that the intensity of the second frequency, f', is at least two orders of magnitude smaller than the magnitude of the fundamental frequency (the amplitude of the oscillation of the streamfunction is however larger in the source region). The instability appears to be weaker at the sink region than at the other locations and also at the sink region there is a long transient during which the signal remains mainly periodic before modulation arises.

The computed value of the azimuthal velocity for $C_w = 132$ at the centre of the cavity is $v = -873$ giving $Ro = 0.475$ at the centre. At $C_w = 133.5$ the solution is still quasi-periodic, with frequencies $f = 81.2$ and $f' = 11.9$.

3.4. *Transition* $QP \rightarrow P5$

When C_w is further increased to 135, the frequencies lock-on to a new regime, denoted $P5$, with a rational relation $f/f' \approx 5$, with $f = 85.2$ and $f' = 16.7$. In figure 8 the dynamical behaviour is shown by Poincaré maps constructed by plotting the values of the streamfunction and of the vorticity at two different locations every time that the streamfunction attains an arbitrary reference value at another location. The reference values used are: in figure 8(a) $\psi(r_2, z_2) = 131.35$, in 8(b) $\psi(r_2, z_2) = 133.2$ and in 8(c) $\psi(r_2, z_2) = 134.3$, and in all cases $\partial\psi/\partial t > 0$. Increasing the mass flow rate up to $C_w = 132$, 133.5, 135 the transition reveals in the Poincaré maps in figure 8: from the QP regime (a) with a non-periodic behaviour in (b), to the P5 regime with the points grouped at five positions in (c). When C_w is decreased there are no traces of hysteresis; for instance, the QP solution is also obtained at $C_w = 133.5$ from the period-five $P5$ solution at $C_w = 135$ and so on. The flow is very similar to the quasi-periodic flow in figure 6. The computed azimuthal velocity at the centre of the cavity is $v = -892.1$ giving $Ro = 0.486$.

3.5. *Transition* $P5 \rightarrow NP$

A further increase of the mass flow rate C_w to 136 leads to a transition to a chaotic regime (NP). The flow is also chaotic at $C_w = 140$ and 150. The streamfunction lines present strong oscillations of the entry zone and some recirculation zones at both sides of the entry wave. Figure 9 has noticeable similarity with the flow visualized by Owen *et al.* (1985). The wavy motion at the entry, and the recirculation zones at the corners are reminiscent of the instabilities which appear in plane symmetric ducts with a sudden expansion (Cherdron, Durst & Whitelaw 1978; Fearn, Mullin & Cliffe 1990).

4. Analysis of the instabilities

In the representation of the instantaneous streamfunction lines it is observed that the unsteady motion is related to a wave in the source region. In this section we will discuss this unsteady motion and we will compare it with other instabilities which present similar features.

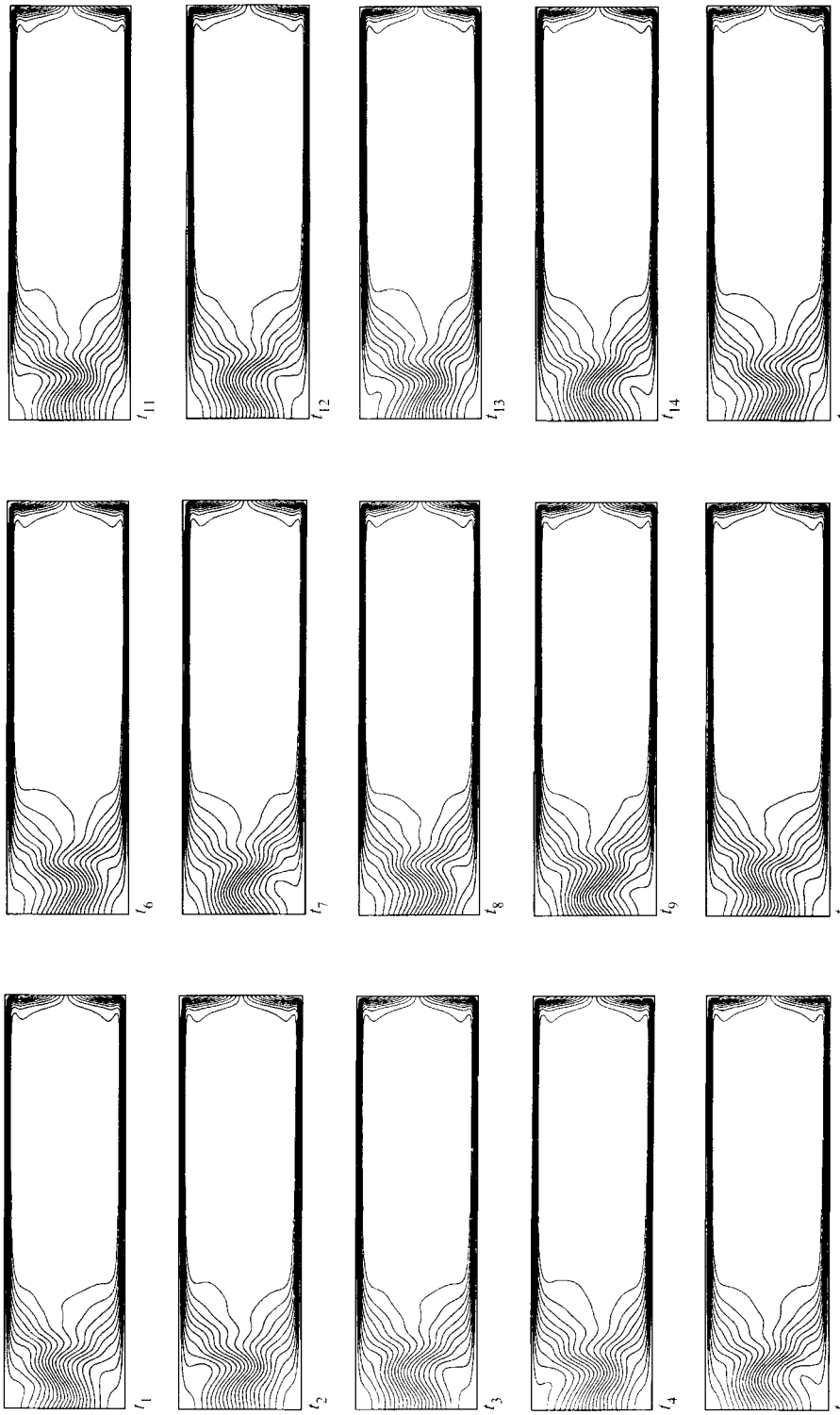

FIGURE 6. Instantaneous plots of the iso-streamfunction lines of the oscillatory flow at different time steps ($t_{i+1} - t_i = 0.56 \times 10^{-2} T$). $C_w = 132$, $E = 2.24 \times 10^{-3}$, $L = 3.37$ and $R_m = 1.22$. The periods are $T = 0.0123$ and $T' = 0.084$ and at the centre of the cavity $Ro = 0.475$. Boundary conditions from (2.8*a*,*b*) at $\tilde{r} = 0.74$ and $\tilde{r} = 7.48$ ($r = \pm 1$).

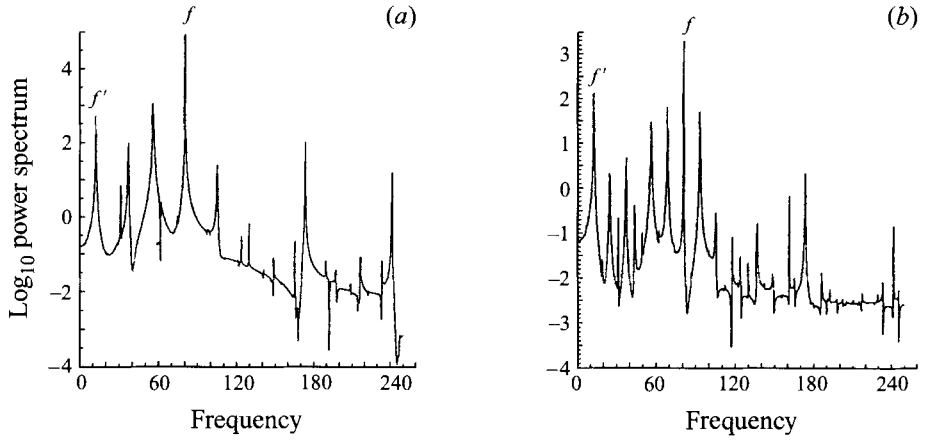

FIGURE 7. Power spectra of the streamfunction at two locations in the cavity: (*a*) at the centre of the cavity and (*b*) inside the Ekman boundary layer for the flow of figure 6. The frequencies are $f = 81.3$ and $f' = 11.9$.

The instabilities observed by Hide appeared at very low values of the mass flow and rotation rates, $C_w \leqslant 20$ and $E \sim 10^{-1}$ to 1 and their origin is not given; thus we will not discuss them. Owen & Pincombe (1980) and Owen *et al.* (1985) attributed the turbulent flow obtained in their experimental configuration to Ekman-layer instabilities. The parameters characterizing these instabilities are the local Reynolds number, $Re = V_g^* \delta / \nu$, where V_g^* is the local geostrophic velocity, $\delta = (\nu/\Omega)^{1/2}$ the thickness of the boundary layer, and r^* the dimensional radial position, and the local Rossby number defined before, $Ro = V_g^*/(\Omega r^*)$. The waves associated with the instabilities of this boundary layer form a series of horizontal roll vortices whose spacing is related to the depth of the boundary layer (Greenspan 1969). In table 1 there is summary of the results in the literature for the local orientation of these waves with respect to the geostrophic flow, the wavelength and the frequency.

There are two difficulties in the mathematical treatment of the three-dimensional problem. One is the non-axisymmetry and the other is the curvature effect. Some theoretical studies on rotating flows avoid the first difficulty by considering that the wave forms an angle with the geostrophic velocity. For instance the stability analyses of the Ekman boundary layers calculate the critical parameters as a function of the angle (and so the critical angle), but they do not take account of the curvature effects. (For instance, as the predicted critical phase velocity is proportional to the geostrophic velocity, and this depends on the radius ($1/r^*$), then the critical wavelength is also expected to vary with the radius.) Because of our axisymmetry assumption our computations are limited to waves forming an angle of zero with respect to the geostrophic flow, but we may study curvature effects and $Ro \neq 0$. In the limit of large radius, $R_m \rightarrow \infty$, we can compare with linear stability results for $\alpha = 0$. An approach using an azimuthal wavenumber different from zero together with curvature effects might explain the origin of spirals like those observed in the recent experiments of Thomas (1994) who found that patterns of the Ekman layer instability follow a law $n^2 = ReRo$, n being the number of arms of the spiral.

Thus in §4.1 we describe some calculations performed in order to observe the instability of the Ekman boundary layers, to compare with the literature and specifically to understand the unsteady flow in our configuration in §3. The relevance of the

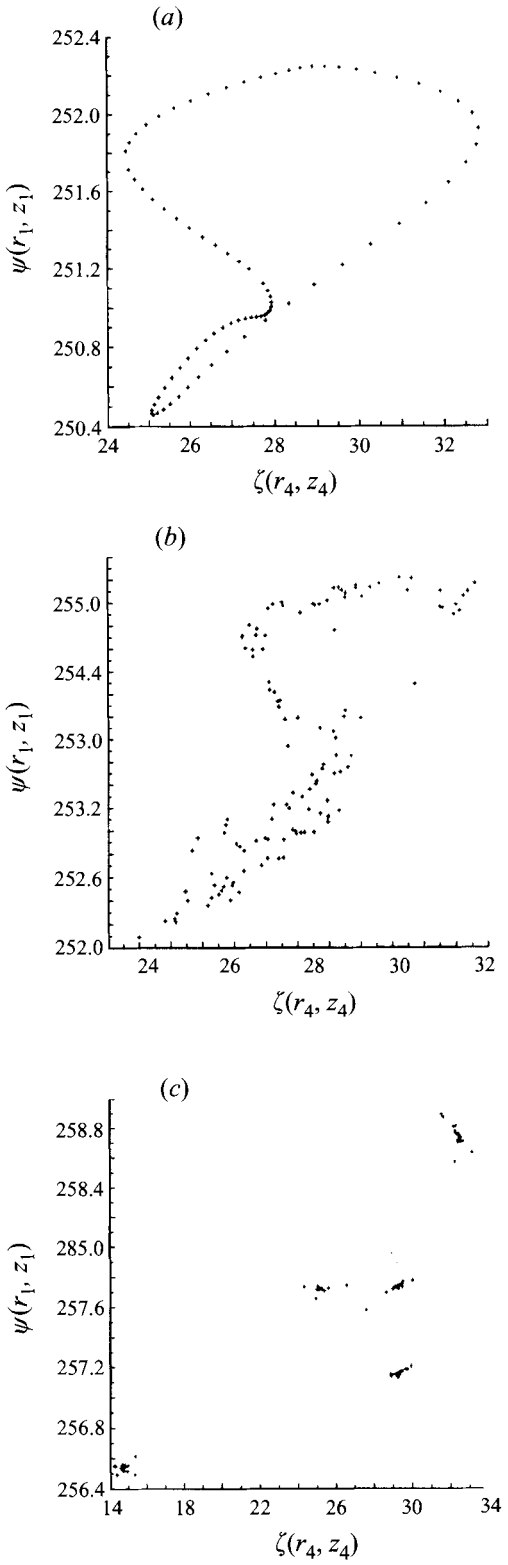

FIGURE 8. Poincaré maps constructed with the streamfunction at the sink region, $\psi(r_1, z_1)$, and the vorticity at the source region, $\xi(r_4, z_4)$. (*a*) Quasi-periodic regime at $C_w = 132$ (parameters as in figure 6), (*b*) $C_w = 133.5$ and (*c*) period-five regime at $C_w = 135$.

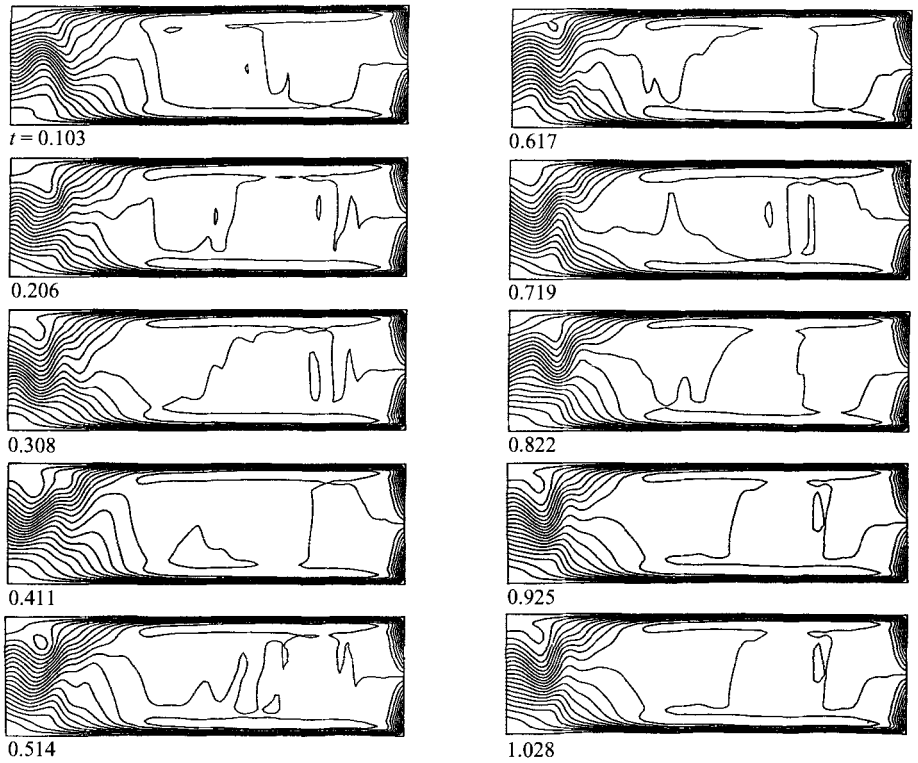

FIGURE 9. Instantaneous iso-streamfunction lines of the non-periodic flow for $C_w = 140$, $E = 2.24 \times 10^{-3}$, $L = 3.37$ and $R_m = 1.22$. Boundary conditions from (2.8*a*,*b*) at $\tilde{r} = 0.74$ and $\tilde{r} = 7.48$ ($r = \pm 1$).

Ekman boundary layers and of the inner region is discussed in §§4.1 and 4.2. Finally we discuss other instabilities such as vortex shedding during a sudden expansion of the flow in a channel and vortex breakdown in a rotating annulus with a forced flow entering axially. Although these situations are different from the one studied here, in all of them the instabilities are excited at the entry.

4.1. *Instability of the Ekman layers*

Experiments on rotating flows (see table 1) have revealed two different instabilities of the Ekman layers, called type II and I (or *A* and *B*). The type I instability is associated with an inflexion point in the velocity profile of the basic flow and the type II instability involves Coriolis and centrifugal forces rather than the inflexion point (Lilly 1966; Faller 1991). The empirical relationship for the critical parameters of type II waves is approximately $(Re)_c^{II} = 56.3 + 58.4\,Ro$. These waves develop first and are very sensitive to the value of *Ro*. The relationship for the critical parameters for type I instabilities is: $(Re)_c^{I} = 124.5 + 3.66\,Ro$. Using the zero-order solution for the azimuthal velocity, (equation (3.1)) the Reynolds and Rossby numbers at a given position, r^*, are: $Re \simeq -Q/(2\pi r^* \nu)$ and $Ro \simeq -Q/[2\pi(\nu\Omega)^{1/2}(r^*)^2]$. Note that the Reynolds and Rossby numbers so defined are negative but for convenience they will be treated as positive numbers; these minus signs only account for the fact that azimuthal velocity goes against rotation in the rotating frame of reference.

In order to understand the appearance of these instabilities in our axisymmetric modelling, we performed some computations using Ekman profiles and the

geostrophic velocity from equation (3.1) as boundary conditions, at $\tilde{r} = 13.48$ and $\tilde{r} = 20.22$. The use of these boundary conditions prevents the instabilities of the entry flow. We considered almost the same configuration $L = 3.37$ and rotation rate, but in this case we used the curvature parameter $R_m = 5$ ($\tilde{r} \in [13.48, 20.21]$) in order to diminish the nonlinear terms, characterized by Ro. This situation is closer to the experimental conditions used to study Ekman-layer instabilities.

The final steady flow in this cavity is an Ekman-type flow at any $\tilde{r}$ with geostrophic velocity close to the value given by (3.1). Recall that this equation is an asymptotic solution and its accuracy is about 7%. At $C_w = 467$ we obtained an oscillatory motion. The perturbations of the flow are obtained by subtracting the Ekman profile from the computed flow. The resulting instantaneous iso-ψ lines in figure 10 show small vortices near the horizontal walls, which correspond to an Ekman-layer instability similar to those described by Faller (1991) in his figure 7. The different size of the vortices near the inlet and outlet is also due to the geostrophic velocity used in the boundary conditions (from equation (3.1)). Anyway this small discrepancy does not significantly affect the resulting flow in the rest of the cavity.

The computed values of the local Reynolds and Rossby numbers are dependent on the position: at $\tilde{r} = \{13.48, 16.85, 20.22\}$, $Re = \{112, 93, 74\}$ and $Ro = \{0.392, 0.288, 0.174\}$. This position dependence of the Reynolds and Rossby numbers comes from the variation of the geostrophic velocity with the radial position as can be observed in equation (3.1).

In order to compare the physical parameters with the results in the literature, we will scale the wavelength with the boundary layer depth, $\lambda = \lambda^*/\delta$, and the frequency with the rotation rate frequency $\sigma = 2\pi f^*/\Omega$. The comparison of the linear stability results with the observations in the experiments must be done cautiously. The linear stability results provide the λ of the most unstable mode, and its corresponding σ, at each Re (and with $Ro = 0$). However in the experiments, and in numerical computations, the waves are observed at Reynolds numbers far above the critical Re and for $Ro \neq 0$. In the experiments, at a given frequency the flow also showed many different waves with different wavelengths and directions (Caldwell & Van Atta 1970).

In our computations the wavelength decreases slightly with the radius, $\lambda^* \propto 1/r^*$, in a range $\lambda^* \simeq 29\delta$ to 26δ (see table 1). The value of the frequency, $f^* = 456\ \nu/h^2$, is in dimensionless form $\sigma \simeq 6$. The comparison with the previous results is not obvious because the local Reynolds number varies for $13.48 \leqslant \tilde{r} \leqslant 20.22$ in a range $112 \geqslant Re \geqslant 74$. But it appears to be compatible with the frequency obtained by Caldwell & Van Atta.

The reported theoretical values of frequencies for type I and II waves for the most unstable mode (Lilly 1966) are, at $Re = 65$, $\sigma \simeq 12$ (type II) and at $Re = 110$, $\sigma \simeq 14$ (type II) and $\sigma \simeq 5$ (type I). The frequencies in the experiments by Caldwell & Van Atta are obtained far above the critical Re, after the perturbations have grown for some time, thus having many wavelengths and different directions. In the range $110 < Re < 250$, they report a linear dependence of the frequency: $7 < \sigma < 12$. These authors observed that the frequency increased with increasing Reynolds number, as in Lilly's calculation for type II instability; this observation supported their conclusion that their instability is type II.

The vortices travel in the radial direction with a phase speed $V_\phi^* = 0.28\, V_g^*$ (see figure 10 and table 1). The phase speed of the instability does not depend on the location.

Summarizing, the parameters which characterize the instability, i.e. the wavelength, the phase velocity and the frequency are not easily comparable with the values in the

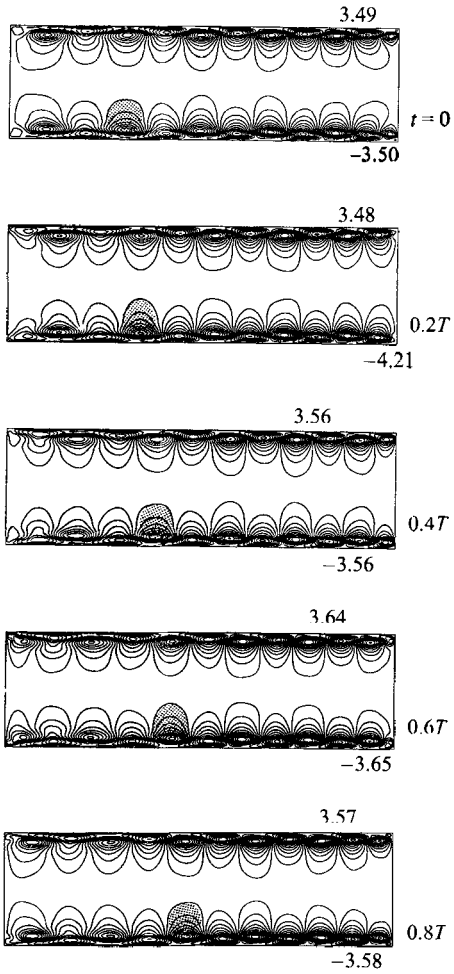

FIGURE 10. Perturbations of the streamfunction of the oscillatory flow for $C_w = 467$, $E = 2.24 \times 10^{-3}$, $L = 3.37$. Ekman-layer-type profiles are used as boundary conditions at the inlet and outlet: $\tilde{r} = 13.48$ and $\tilde{r} = 20.22$ ($r = \pm 1$, $R_m = 5$). The period is $T = 0.0022$ and at the centre of the cavity $Ro = 0.29$ (in which case $13.5 \leqslant r^*/h \leqslant 20.22$). The location of half a vortex is marked at different instants.

literature. For instance the wavelength varies with the position as $\lambda^* \propto 1/r^*$, i.e. it does depend on the local Re and Ro. Otherwise the frequency and the phase velocity, V_ϕ^*/V_g^*, do not vary with the position. Like the results from Maubert *et al.* (1992) and Maubert (1993) for $R_m = 13.94$ and constant C_w, the frequency seems to vary as $f \propto E$.

These unknown dependencies $\lambda^* = \lambda^*(Re, Ro)$ and $f = f(C_w, E)$ make the comparison with the values in the literature difficult.

4.2. *Instability of the entry flow*

Going back to the results obtained in §3 using a Poiseuille-type profile as boundary conditions at the vertical boundaries, we will discuss here in detail the flow associated with the time-dependent behaviour. In §3 we have described the transitions of the steady flow to time-dependent flows at increasing C_w: the first instability, $S \rightarrow P1$, is observed at $C_w = 120$ corresponding to the local parameters at $\tilde{r} = 4.11$: $Ro = 0.43$

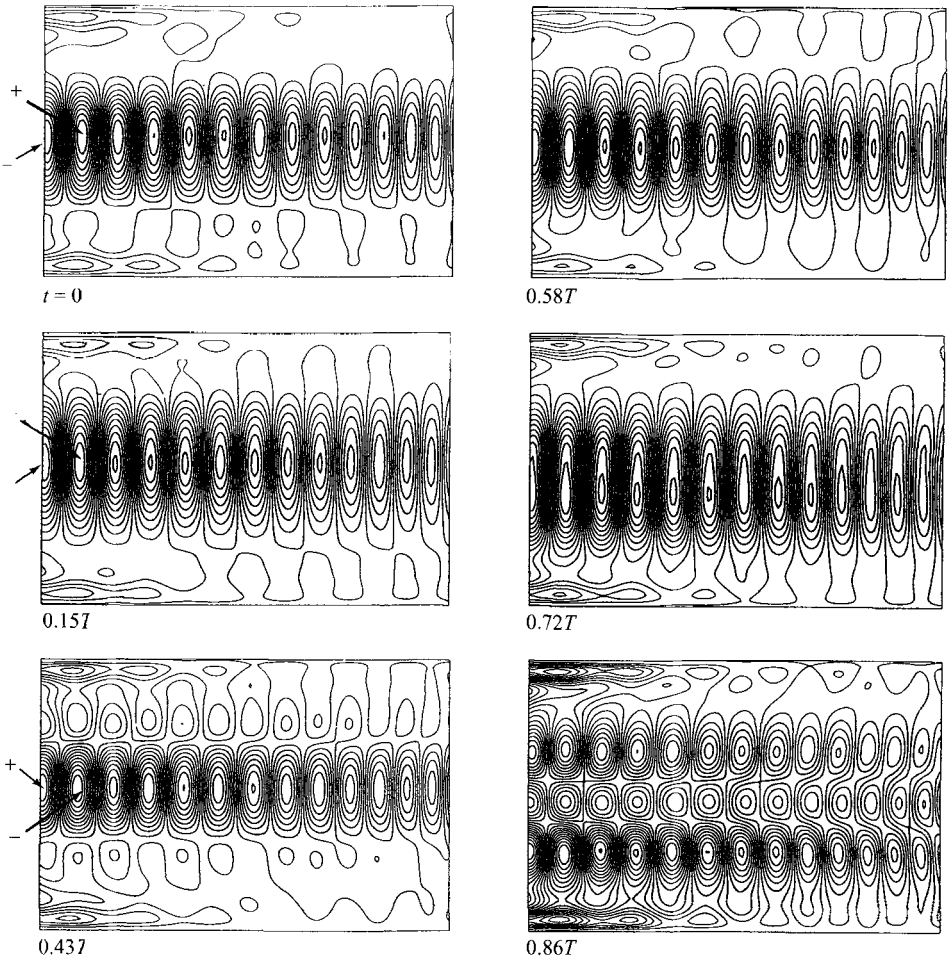

FIGURE 11. Perturbations of the vertical velocity component of the flow at $C_w = 120$ (flow of figure 5) in the core region ($4.11 < \tilde{r} < 7.14$ and $-1 < z < 1$)

and $Re = 38$ (at the centre of the cavity). At $C_w = 135$, the local parameters at $\tilde{r} = 4.11$ are $Ro = 0.49$ and $Re = 42$. These values of the Reynolds number are smaller than the critical value for Ekman-layer instabilities obtained by experiments and stability theory: $Re_c \geqslant 55$.

In order to check if the previous results in §3 could also be related with the Ekman-layer instabilities we observe this region carefully. Subtracting the main flow (we used the steady computed flow) from the total flow at $C_w = 120$, some vortices are visible near the Ekman layers and also in the core region. In figure 11 the perturbations correspond to the flow in figure 5 (we have removed the source and sink regions). During a period, the perturbations in the core region connect both horizontal layers.

Owen & Pincombe (1980) and Owen *et al.* (1985) described the instabilities observed in their visualization as "weak instabilities in the 'developed ' Ekman layers adjacent to the potential core and large-scale instabilities in the 'developing' Ekman layers inside the inner layer. These large-scale instabilities give rise to unsteady flow throughout the inner layer" (see Owen & Pincombe 1980). Their instability criterion was arbitrary: in Owen & Pincombe (1980) they used 'the radius at which the ripples

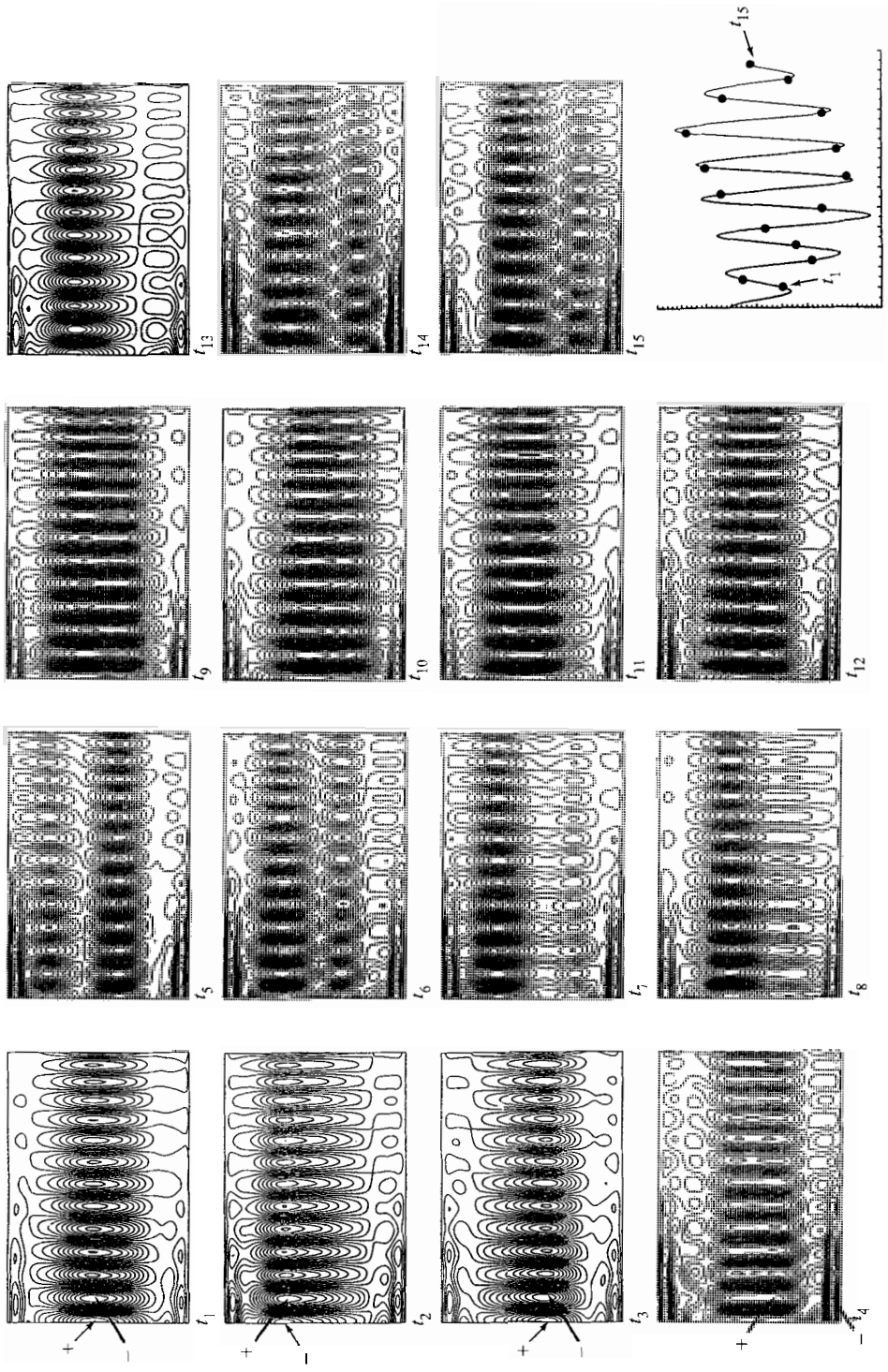

FIGURE 12. Perturbations of the vertical velocity component of the quasi-periodic flow for $C_w = 132$ (flow of figure 6) in the core region: $4.11 < \tilde{r} < 7.14$ and $-1 < z < 1$ at several instants ($t_{i+1} - t_i = 0.56 \times 10^{-2} T$), with $T = 0.0123$ and $T' = 0.084$.

in the boundary of the Ekman layer could no longer be discerned with the naked eye', and in Owen *et al.* (1985) they observed that 'the tangential component of velocity measured in the core departed significantly from that predicted by the linear theory for laminar flow'; however both criteria gave similar values of the critical parameters (10%). They concluded that transition from laminar to turbulent flows takes place at $Re \approx 180$. Although these authors have not carefully studied the entry flow, their description is consistent with the features we have observed in our unsteady flow (at lower values of C_w and Re because the numerical method allows us to have sensitiveness very near the onset of the instability).

The frequency of the oscillatory motion, $P1$, is close to the rotation frequency of the cavity, $\sigma = 1.14$. This fact is characteristic of inertial waves, which occur in rotating flows with frequency values ranging from zero to 2σ. The frequency obtained by Tatro & Mollö-Christensen who also used a low curvature parameter is $\sigma \simeq 1$, and it has been shown by Cerasoli (1975) that their instability was excited by the test probe. In our numerical studies the instability is excited by the entry flow which induces perturbations in the Ekman layers that decay gradually in the radial direction (the local Reynolds number decays in the same direction). No change of the pattern flow is observed in the quasi-periodic regime in figure 6 which could be associated with the onset of the second frequency. The disturbances of the streamfunction in the core region $4.11 \leqslant \tilde{r} \leqslant 7.14$ are presented in figure 12. The frequency f' is of the same order as the inverse of the spin-up time, and it is seen with more intensity in the spectrum of the signal at the Ekman layer, suggesting the hypothesis that it is related with the time of decaying for the perturbations at the boundary layers. However the reason why this frequency appears only for high mass flow rates (or local Reynolds numbers) is not well understood.

4.3. *Similarity with other instabilities*

Because the instability is observed at the source region, we have searched in the literature for experiments in forced flows showing similarities in flow visualizations and also in the physical conditions.

We discuss the visualizations of the flow in a two-dimensional plane channel after a sudden expansion obtained by Cherdron *et al.* (1978) and also Fearn *et al.* (1990) (see the figure 11 of the second paper). In this case the steady flow displays symmetry about the midplane of the channel with two identical regions of recirculating flow behind the steps of the expansion. On increasing the velocity at the entry, the flow becomes asymmetric (steady). On further increasing the velocity at inlet, a third recirculating zone appears attached to one of the walls. At this stage the flow is oscillatory, the vortices being shed periodically from the top (bottom) shear layer at the downstream end of the third recirculation zone. This description of the mechanism fits with our results shown in the figure 9, where a recirculation zone is seen alternately at the top and bottom of the entry flow. Also in our rotating cavity the Poiseuille flow at the entry expands somewhat while readjusting to the flow in the core region, i.e. a geostrophic region and two Ekman boundary layers. The controlling parameter in a sudden expansion is the critical Reynolds number based on the maximum inlet velocity and the upstream channel height, and the onset of oscillatory motion is predicted theoretically (and confirmed by the experiments) at an equivalent $C_w = 120$. The frequency at $C_w = 128$ is $f \simeq 4$, i.e. of the order of the viscous diffusion time.

A vortex breakdown phenomenon is described by Owen & Pincombe (1979), who studied experimentally a rotating cavity with a jet entering in the direction of the axis of rotation. At the lower values of the entry flow, they observed occasional flow

reversal at the downstream end of the jet. This behaviour is termed the axisymmetric vortex breakdown mode, and has a frequency $2\pi f^*/\Omega = 1$. (Note that is the same as we found in our first transition; also very small reversal flows are observed at the sides of the entry flow, and they are evident in the quasi-periodic flow in figure 6.) This axisymmetric vortex breakdown mode occurred in the experiments for low values of the Rossby number. At higher values of the Rossby number they found a spiral breakdown mode.

5. Summary and conclusions

We have investigated the axisymmetric instabilities which appear in a source–sink rotating flow at high rotation rate, $E = 2.24 \times 10^{-3}$. In this configuration the structure of the flow comprises four separate regions which are very similar before and after the transition to unsteady motion, as has been observed in experiments (see §4). Thus, an instability of the entry flow with an azimuthal wavenumber is not expected to behave differently from the axisymmetric one considered here. The restriction to an angle $\alpha = 0$ in the study of the instability of the Ekman boundary layers has been discussed in §4.1 and the qualitative spatial and dynamical behaviours seem well represented. Moreover, there may be a range of parameters for low Rossby number where the instability of the entry flow is axisymmetric, as is the case of the vortex breakdown described by Owen & Pincombe (1979).

In most of the computations we have considered a cavity with small radius of curvature, $R_m = 1.22$. In that case the local Rossby number is high, $Ro \simeq 0.36$ to 0.49, favouring the appearance of inertial waves excited by the entry flow. We have performed computations in a cavity with $R_m = 5$ (giving $Ro \simeq 0.29$), using an Ekman-type profile as boundary conditions to get an insight into the instabilities of the Ekman boundary layers and we have used this information to elucidate different aspects of our instability, presented in §3.

We summarize the results for the cavity with a Poiseuille-type profile at the source and sink and for a small radius of curvature. The steady solutions obtained for $C_w \leqslant 100$ agree with previous experimental and numerical results in the literature. The flow is symmetric with respect to the midheight plane, $z = 0$, and the transition to oscillatory motion breaks this symmetry. For $C_w \geqslant 120$ the flow is time-dependent; however, the main flow maintains the same global structure and the instabilities are relatively weak perturbations of the main flow. In particular at $C_w = 120$ the flow is oscillatory and the patterns of the streamfunction reveal oscillations at the entry zone. When the basic (steady) flow is subtracted from the total flow, the perturbations of the streamfunction are vortices along the Ekman boundary layers and horizontal waves in the core region connecting the vortices. The amplitude of the vortices decreases gradually in the radial direction (as could be expected from the dependence $Re \propto \tilde{r}^{-1}$) and varies with time. The wavelength of the perturbations decreases in the radial direction also. The frequency of the oscillatory motion is close to the rotation rate frequency of the cavity, suggesting an inertial wave in a rotating fluid. At $C_w = 132$, the flow becomes quasi-periodic. The analysis of the corresponding spatial pattern does not reveal any qualitative difference with the periodic flow. A plausible explanation for the second frequency, which has a value close to the Ekman or spin-up characteristic time, is that it is related to the decaying time for perturbations. This behaviour would not be observed in the figures for the quasi-periodic regime (figures 6 and 12) because the period of this decaying is about five times the period of the entry wave, which has stronger intensity. The values of the frequencies and

wavelengths, together with the images of the flow support the hypothesis that the entry wave has an inertial nature and excites the vortices at the Ekman layers which, due to the low value of the local Reynolds number, are unstable and damped.

Using Ekman layer profiles as boundary conditions at the source and sink, in a cavity with a larger radius of curvature, we have investigated the appearance of instabilities of the Ekman boundary layers in §4.1. We have obtained an oscillatory motion associated with perturbations along the boundary layers. These perturbations are vortices and are visualized as waves in the total flow in the experiments (Faller 1991). Although the actual flow is three-dimensional, the major features of the instability can be understood by considering an axisymmetric flow. The parameters of the unstable flow, such as Reynolds and Rossby numbers, frequency, wavelength are consistent with the results available in the literature. In principle, these values suggest that it could be the case of an Ekman layer instability of type II. But the unknown dependence of the wavelength on the local parameters, $\lambda(Re, Ro)$ and of the frequency (or phase velocity) on the rotation rate $f(E, C_w)$ does not allow us to conclude whether it is a type II or type I instability. In any case the result confirms unambiguously that the instabilities studied in §3 are not instabilities of the Ekman layers.

The computations were carried out on both CRAY YMP2E and CRAY C98 computers with support from IMT (Château-Gombert, Marseille) and Conseil Régional PACA, and from IDRIS/CNRS (Orsay), respectively. The authors are indebted to Professor M. A. Rubio (UNED, Madrid) for his valuable comments throughout the course of this work. The authors are also grateful to Dr A. M. Chaouche for writing the numerical code and to Professor J. M. Owen (University of Bath), Professor J. C. Antoranz (UNED, Madrid) and Professor R. L. Sani (University of Boulder, Colorado) for fruitful discussions. The research was supported by DGA, DRET (Groups 6 and 7), SNECMA (Group YKL), GDR MFN (CNRS), Conseil Régional PACA, Intl. Exchange Progs. and Ministère des Affaires Etrangères (France) and CICYT PB93-0293 and PB94-0382 contracts, Acción Integrada Hispano-Francesa 52B contracts (Spain).

REFERENCES

BENNETTS, D. A. & JACKSON, W. D. N. 1974 Source–sink flows in a rotating annulus: a combined laboratory and numerical study. *J. Fluid Mech.* **66**, 689–705.

CALDWELL, D. R & VAN ATTA, C. W. 1970 Characteristics of Ekman boundary layer instabilities. *J. Fluid Mech.* **44**, 79–95.

CANUTO , C., HUSSAINI, M. Y., QUARTERONI, A. & ZANG, T. A. 1988 *Spectral Methods in Fluid Dynamics*. Springer.

CERASOLI, A. P. 1975 Free shear layer instability due to probes in rotating source–sink flow. *J. Fluid Mech.* **72**, 559–586.

CHAOUCHE, A. M. 1990 Une méthode de collocation-Chebyshev pour la simulation des écoulements axisymétriques dans un domaine annulaire en rotation. *La Recherche Aérospatiale* **5**, 1–13.

CHAOUCHE, A., RANDRIAMAMPIANINA A. & BONTOUX, P. 1990 A collocation method based on an influence matrix technique for axisymmetric flows in an annulus. *Comput. Meth. Appl. Mech. Engng* **80**, 237–244.

CHERDRON, W., DURST, F. & WHITELAW, J. H. 1978 Asymmetric flows and instabilities in symmetric ducts with sudden expansions. *J. Fluid Mech.* **84**, 13–31.

CHEW, J. W., OWEN, J. M. & PINCOMBE, J. R. 1984 Numerical predictions for laminar source–sink flow in a rotating cylindrical cavity. *J. Fluid Mech.* **143**, 451–466.

EHRENSTEIN, U. & PEYRET, R. 1989 A Chebyshev-collocation method for the Navier–Stokes equations with applications to double-diffusive convection. *Intl J. Numer. Meth. Fluids* **9**, 427–452.

FALLER, A. J. 1963 An experimental study of the instability of the laminar Ekman boundary layer. *J. Fluid Mech.* **15**, 560–576.

FALLER, A. J. 1991 Instability and transition of disturbed flow over a rotating disk. *J. Fluid Mech.* **230**, 245–269.

FALLER, A. J. & KAYLOR, R. E. 1966 A numerical study of the instability of the laminar Ekman boundary layer. *J. Atmos. Sci.* **23**, 466–480.

FEARN, R. M., MULLIN, T. & CLIFFE, K. A. 1990 Nonlinear flow phenomena in a symmetric sudden expansion. *J. Fluid Mech.* **211**, 595–608.

GOTTLIEB, D. & ORSZAG, S. A. 1977 *Numerical Analysis of Spectral Methods: Theory and Applications.* CBMS-SIAM Publications.

GREENSPAN, H. P. 1969 *The Theory of Rotating Fluids.* Cambridge University Press.

HAIDVOGEL, D. B. & ZANG, T. A. 1979 The accurate solution of Poisson equation by expansion in Chebyshev polynomials. *J. Comput. Phys.* **30**, 137–180.

HIDE, R. 1968 On source-sink flows in a rotating fluid. *J. Fluid Mech.* **32**, 737–764.

HOPFINGER, E. J. & LINDEN, P. F. 1990 The effect of background rotation on fluid motions: a report on Euromech 245. *J. Fluid Mech.* **211**, 417–435.

HYUN, J. M. 1984 Source–sink flows of a stratified fluid in a rotating annulus. *J. Fluid Mech.* **145**, 111–125.

IOOSS, G., NIELSEN H. B. & TRUE, H. 1978 Bifurcation of the stationary Ekman flow into a stable periodic flow. *Arch. Rat. Mech. Anal.* **68**, 227–256.

KLEISER, L. & SCHUMANN, U. 1980 Treatment of incompressibility and boundary conditions in 3D numerical spectral simulations of plane channel flows. In *Numerical Methods in Fluid Mechanics* (ed. E. H. Hirschel), pp. 165–173. Vieweg.

LE QUÉRÉ, P. & PÉCHEUX, J. 1989 Numerical simulations of multiple flow transitions in axisymmetric annulus convection. *J. Fluid Mech.* **206**, 517–544.

LILLY, D. K. 1966 On the instability of Ekman boundary flow. *J. Atmos. Sci.* **23**, 481–494.

MAUBERT, P. 1993 Etude de régimes d'écoulements et de transferts thermiques dans les systèmes en rotation soumis à un flux forcé. Doctorate thesis, Université d'Aix-Marseille II, France.

MAUBERT, P., CHAOUCHE, A. M., CRESPO DEL ARCO, E. & BONTOUX, P. 1992 Régimes d'écoulements instationnaires dans une cavité annulaire tournante soumise à un flux radial forcé. *C. R. Acad. Sci. Paris* **315**, S.II, 1593–1600.

ORSZAG, S. A. & KELLS, L. C. 1980 Transition to turbulence in plane Poiseuille and plane Couette flow. *J. Fluid Mech.* **96**, 159–205.

OUAZZANI, J. 1984 Méthode pseudo-spectrale pour la résolution des équations d'un mélange de gaz binaire. Doctorate thesis, Université de Nice, France.

OWEN, J. M. & PINCOMBE, J. R. 1979 Vortex breakdown in a rotating cylindrical cavity. *J. Fluid Mech.* **90**, 109–127.

OWEN, J. M. & PINCOMBE, J. R. 1980 Velocity measurements inside a rotating cavity with a radial outflow of fluid. *J. Fluid Mech.* **99**, 111–127.

OWEN, J. M., PINCOMBE, J. R. & ROGERS, R. H. 1985 Source–sink flow inside a rotating cylindrical cavity. *J. Fluid Mech.* **155**, 233–265.

PULICANI, J. P., CRESPO DEL ARCO, E., RANDRIAMAMPIANINA, A., BONTOUX, P. & PEYRET, R. 1990 Spectral simulations of oscillatory convection at low Prandtl number. *Intl J. Numer. Meth. Fluids* **10**, 481–517.

SAVAS, O. 1987 Stability of Bödewadt flow. *J. Fluid Mech.* **183**, 77–94.

SCHLICHTING, H. 1960 *Boundary Layer Theory.* McGraw Hill.

TATRO, P. R. & MOLLÖ-CHRISTENSEN, E. L. 1967 Experiments on Ekman layer instability. *J. Fluid Mech.* **28**, 531–543.

THOMAS, P. J. 1994 Pattern formation of granules on the bottom of a differentially rotating tank. *J. Fluid Mech.* **274**, 23–41.

VANEL, J. M., PEYRET, R. & BONTOUX, P. 1986 A pseudo-spectral solution of vorticity streamfunction equations using the influence matrix technique. In *Numerical Methods for Fluids Dynamics II* (ed. K. W. Morton & M. J. Baines), pp 463– 475. Clarendon Press.

WEIDMAN, P. D. 1976 On the spin-up and spin-down of a rotating fluid. Part 2. Measurements and stability. *J. Fluid Mech.* **77**, 709–735.